IMPACT OF ON-BOARD HYPERSPECTRAL DATA COMPRESSION ON MINERAL MAPPING PRODUCTS

K. Staenz[a)], R. Hitchcock[b)], S. Qian[c)], and R.A. Neville[a)]
[a)]Canada Centre for Remote Sensing, Natural Resources Canada, 588 Booth Street, Ottawa, ON, Canada K1A 0Y7 (karl.staenz@ccrs.nrcan.gc.ca)
[b)]Prologic Systems Ltd., 75 Albert Street, Suite 206, Ottawa, ON, Canada (robert.hitchcock@ccrs.nrcan.gc.ca)
[c)]Canadian Space Agency, 6767 Route de l'Aéroport, St. Hubert, QC, Canada J3Y 8Y9 (Shen-en.Qian@space.gc.ca)

Commission VII, WG VII/1

KEY WORDS: Hyperspectral, Geology, Compression, Processing, Classification, Impact Analysis

ABSTRACT:

As on-board data compression is an option for future operational hyperspectral satellite systems, its impact on the data products need to be investigated. Accordingly, the study presented in this paper investigated the impact of lossy Hierarchical Self-organizing Cluster Vector Quantification (HSOCVQ) data compression on the identification and mapping of minerals in environments with sparse vegetation cover. For this purpose, an Airborne Visible/Infrared Imaging Spectrometer (AVIRIS) radiance cube acquired over the Cuprite mining district area in Nevada on June 12, 1996 was compressed by factors of 10, 20, and 40. The original data and the de-compressed data were processed separately, applying atmospheric correction using MODTRAN4.2 and spectra post-processing prior to automatic Iterative Error Analysis (IEA) endmember selection, and subsequent constrained spectral linear unmixing to produce mineral (endmember) abundance maps. The results indicate that the errors between original radiance data and de-compressed data increase with increasing compression ratio. This trend is also true for the derived mineral abundance maps. In general, for most of the endmembers, the 10:1 and 20:1 compression ratios produced abundance maps which are spatially similar to those extracted from the original data, when only fractions larger than 0.5 are mapped. Only these higher fractions are of interest for exploration purposes. One endmember out of 15 was lost using the 40:1 compression ratio and, consequently, this particular endmember could not be mapped.

1.0 INTRODUCTION

With the launch of spaceborne hyperspectral sensors, data transmission becomes an issue due to the high data rate required to cope with the large volumes of hyperspectral data. This is especially true when moving towards operational systems, as compared to technology demonstrators such as NASA's Hyperion. In order to overcome this problem, lossy data compression can be used to reduce the data volume while preserving enough information for the generation of application products in various areas, such as forestry, agriculture, environment, coastal/inland waters, and geoscience. Suitable data compression techniques are those which use Vector Quantization (VQ) (Qian et al., 1997 and 2000). These techniques are characterised by their near lossless property with high compression ratio and relatively simple structure.

The goal of this study is to apply a VQ compression technique, called the "Hierarchical Self-organizing Cluster Vector Quantification" (HSOCVQ: Qian et al., 2002), to calibrated (radiance) hyperspectral airborne data to investigate the impact of this technique on mineral mapping products. For this purpose, an Airborne Visible/Infrared Imaging Spectrometer (AVIRIS: Green et al., 1998) data set acquired on June 12, 1996 over a test site near Cuprite, Nevada, U.S.A., was used.

The products retrieved from data compressed with HSOCVQ were compared quantitatively and qualitatively with the products extracted from the original (uncompressed) data. The ratios used in the compression are 10:1, 20:1, and 40:1. The subsequently de-compressed data sets were processed in the same way as the original data. Major processing steps include the removal of atmospheric effects, automatic extraction of endmembers, and application of a constrained linear spectral unmixing technique to map the minerals. These processing steps were carried out using the Imaging Spectrometer Data Analysis System (ISDAS: Staenz et al., 1998) developed at the Canada Centre for Remote Sensing. The paper describes in detail the aforementioned processing steps together with the extracted results. Special emphasis is given to the analysis of the end products (fractions of minerals), but also to the comparison of intermediate outputs such as the endmembers.

2.0 DATA USED

A Cuprite standard Jet Propulsion Laboratory (JPL) AVIRIS data set, collected on June 12, 1996, has been used for this study. This sensor acquires imagery at approximately 20-m ground resolution from an ER-2 aircraft in 224 spectral bands, each about 10 nm wide, in the 400-nm to 2500-nm wavelength range. Additional information for identification of endmembers includes the USGS (2002) spectral data base.

The site selected for this study lies within the Cuprite mining district of Nevada (37.6^0 N and 117.2^0 W). This site has been used as a test area for mineral mapping in hyperspectral remote

sensing for many years (Goetz and Srivastava, 1985; Hook and Rast, 1990; Swayze et al., 1992; Neville et al., 2003). Accordingly, this site is very well characterized in terms of mineralogy. This and the excellent exposure of alteration minerals such as alunite, kaolinite, buddingtonite, and others together with limited soil development and sparse vegetation make this area an ideal test site for evaluation of the impact of data compression on mineral abundance maps.

3.0 DATA PROCESSING

An outline of the data processing is given in Figure 1. The different steps include data compression and de-compression, atmospheric correction and post-processing of spectra, endmember selection and spectral unmixing, and fidelity assessment. The original data and de-compressed data cubes are processed separately using the same data processing techniques.

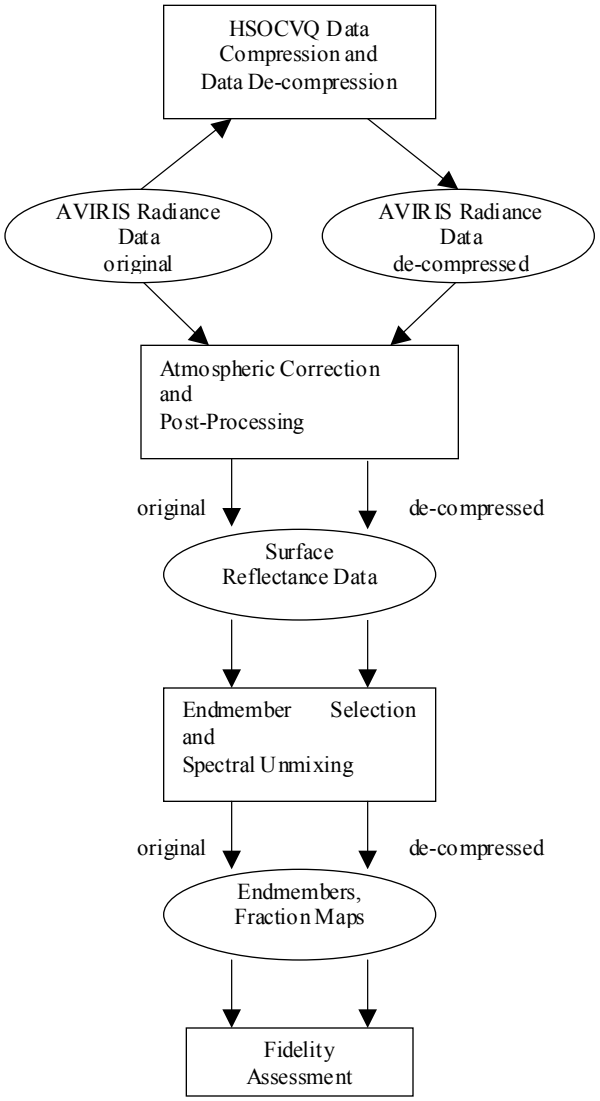

Figure 1. Data processing scheme

3.1 Data Compression

The AVIRIS radiance data cube was compressed by factors of 10, 20, and 40 with the HSOCVQ, which is a VQ based data compression technique with a characteristic of self-organising clusters. This technique clusters spectra in the data cube while it compresses them. It applies VQ to each of the clusters and ensures each of the vector-quantized clusters to have a fidelity better than the given threshold. If the fidelity of the cluster is not better than the threshold, the spectra in the cluster are adaptively re-clustered. As a result of the unique way of clustering, the code vectors trained in this process are very fast and efficient. High reconstruction fidelity can be attained with a relatively small codebook. One of the unique features of this technique is the guarantee that the reconstruction fidelity of each spectrum in the compressed data cube is better than the threshold. This feature allows HSOCVQ to preserve spectral signatures of small targets in the scene of a hyperspectral data cube. Subsequently, the compressed data were de-compressed in order to reconstruct the cubes using the codebooks generated for each cluster.

3.2 Surface Reflectance Retrieval

Prior to the correction of the atmospheric effects, the wavelengths covering the strong atmospheric water absorption regions at 1380 nm and 1870 nm were eliminated from further processing due to the dominance of noise in these areas. For the same reason, the first six bands and the last five bands were also excluded resulting in a reduced wavelength coverage of 428 nm to 2458 nm.

Surface reflectances were then computed from at-sensor radiance (original) data and de-compressed data cubes, compensating for atmospheric absorption and scattering effects. The procedure is based on a look-up table (LUT) approach with tunable breakpoints as described in Staenz and Williams (1997), to reduce significantly the number of radiative transfer (RT) code runs. MODTRAN4.2 was used in forward mode to generate the radiance LUTs, one each for a 5% and 60% reflectance. These LUTs were produced for five pixel locations equally spaced across the swath, including nadir and swath edges, for a range of water vapour contents, and for single values of aerosol optical depth (horizontal visibility) and terrain elevation. The specification of these parameters and others required for input into the MODTRAN4.2 RT code are listed in Table 1.

Atmospheric model	US standard 76
Aerosol model	Desert
Date of overflight	June 12, 1996
Solar zenith angle	15.8°
Solar azimuth angle	153.7°
Sensor zenith angle	Variable
Sensor azimuth angle	Variable
Terrain elevation (above sea level)	1.524 km
Sensor altitude (above sea level)	20.100 km
Water vapour content	variable
Ozone column CO_2 mixing ratio	as per model 300 ppm
Horizontal visibility	50 km
Wavelength grid interval	1 cm^{-1}

Table 1. Input parameters for MODTRAN4 code runs

For the retrieval of the surface reflectance, the LUTs were adjusted only for the pixel location in the swath and water vapour content using a bi-linear interpolation routine (Press et al., 1992) since single values for the other LUT parameters were used for the entire cube. For this purpose, the water vapour content was estimated for each pixel in the scene with an iterative curve fitting technique (Staenz et al., 1997). The surface reflectance was then computed for each pixel as described in Staenz and Williams (1997).

The next processing step performs an empirical correction for irregularities in the reflectance data (band-to-band errors) that may have originated in the sensor, or that may have resulted from the approximation made in atmospheric modelling and the selection of RT code input parameters. These band-to-band errors were removed by calculating correction gains and offsets using spectrally flat targets (Staenz et al., 1999). The removal of these errors is referred to as post-processing.

3.3 Endmember Selection and Spectral Unmixing

Endmembers, required for the spectral unmixing, were selected from the data cubes themselves using an automated method, the Iterative Error Analysis (IEA: Szeredi et al., 2002). In a first step, the average spectrum of the scene is used to unmix the data set. When a data set is unmixed, a residual error image is produced. These errors, which are also a measure of the distance in n-dimensional space (n = number of bands) between the average spectrum and all the spectra of the data set, are calculated using a least-square estimate between the average spectrum and the spectrum of each pixel. The next step is to find the pixel or pixels that encompass the largest errors, i.e., that are furthest away from the average spectrum. The user selects the number of pixels forming these endmembers. This first endmember is then used to unmix the image cube, and the average spectrum is discarded. The errors will again be used to find the furthest pixels from the first endmember and will create the second endmember. This process is repeated until the number of endmembers predetermined by the user is reached. In this case, 15 endmembers have been selected.

Once all the endmembers were found, the image cube was unmixed using a constrained linear technique (Shimabukuru and Smith, 1991; Boardman, 1995). Spectral unmixing uses a linear combination of a set of endmember spectra to unmix the composite spectrum into endmember fractions (between 0 and 1) for each pixel of the scene. The reduced (428 nm – 2458 nm) AVIRIS wavelength range was utilised for the endmember selection and spectral unmixing.

4.0 FIDELITY ASSESSMENT

The assessment of the fidelity between original and de-compressed data was carried out at different data processing levels. The Root Mean Square Error (RMSE) was calculated between original and de-compressed 16-bit digital numbers (scaled radiance) data cubes as follows:

$$RMSE = \sqrt{\frac{1}{n_x\, n_y\, n_b} \sum_{x=1}^{n_x} \sum_{y=1}^{n_y} \sum_{b=1}^{n_b} [DN_D(x,y,b) - DN_O(x,y,b)]^2}\,, \quad (1)$$

where DN_D is the digital number of the de-compressed cube, DN_O is the digital number of the original cube, n_x is total number of pixels in the cube, n_y is the number of lines in the cube, n_b is total number of bands in the cube, x and y are the pixel and line position, respectively and b is the band number.

In addition, the percent relative absolute difference (PRAD) was used as a fidelity measure for spectral variations on a pixel basis between original and de-compressed data. PRAD is defined as follows:

$$PRAD = 100\ \frac{\sqrt{(L_O(x,y,b) - L_D(x,y,b))^2}}{L_O}, \quad (2)$$

where L_o is the radiance of the original spectrum and L_D is the radiance in the de-compressed spectrum. Similarly, PRAD was also calculated for selected bands for all pixels in the scene to show the spatial variability of the data compression of the radiance data.

The assessment of the endmember spectra was carried out using the Average PRAD (APRAD) and Spectral Angle Mapper (SAM; Kruse et al., 1993) as a fidelity measure. These measures can be written as:

$$APRAD = \frac{1}{n_b} \sum_{b=1}^{n_b} PRAD(b) \quad (3)$$

and

$$SAM = \cos^{-1}\left(\frac{\sum_{b=1}^{n_b} em_O(b)\ em_D(b)}{\sqrt{\sum_{b=1}^{n_b} [em_O(b)]^2 \sum_{b=1}^{n_b} [em_D(b)]^2}} \right), \quad (4)$$

where $em_O(b)$ is the endmember reflectance in band b of the original cube and $em_D(b)$ is the endmember reflectance in band b of the de-compressed cube. SAM varies between 0 and 1 where 0 indicates a perfect match between original and de-compressed endmember spectra. While APRAD provides a measure of the overall difference between original and de-compressed endmember spectra, SAM, which is insensitive to gain factors, gives a good indication about the preservation of absorption features in the de-compressed data.

The fraction maps for each of the 15 endmembers were compared using the RMSE.

5.0 RESULTS

5.1 Radiance Data

The RMSE, calculated with equation (1) between original and de-compressed radiance cubes, increases with increasing data compression ratio (Table 2). A similar trend can be observed for the spatial within-band differences between original and de-compressed data expressed via PRAD. As an example, Figure 2 shows the frequency distribution of PRAD, calculated for each pixel of bands 69 (1011 nm) and 205 (2319 nm), for data compression ratios of 10:1, 20:1, and 40:1. Both graphs show the same trend, although larger errors occur in band 205 for all compression ratios. Most pixels, 99.8 % at compression ratios of 10:1 and 99.3 % at 20:1, lie within 2.5 % error for band 69 compared to 69.1 % and 65.3 %, respectively, for band 205.

Compression Ratio	10:1	20:1	40:1
RMSE	33.64	50.57	60.75

Table 2. RMSE of the original (average DN_O = 4960) and de-compressed data cubes for different compression ratios. DN_O and RMSE are in DN (scaled radiance).

For the same error margin, the number of pixels decreases to 97.5 % (band 69) and 56.3 % (205) for a compression ratio of 40:1. A 6.5-% error margin in band 205 includes 95.8 % (10:1), 94.2% (20:1), and 89.7% (40:1) of the pixels.

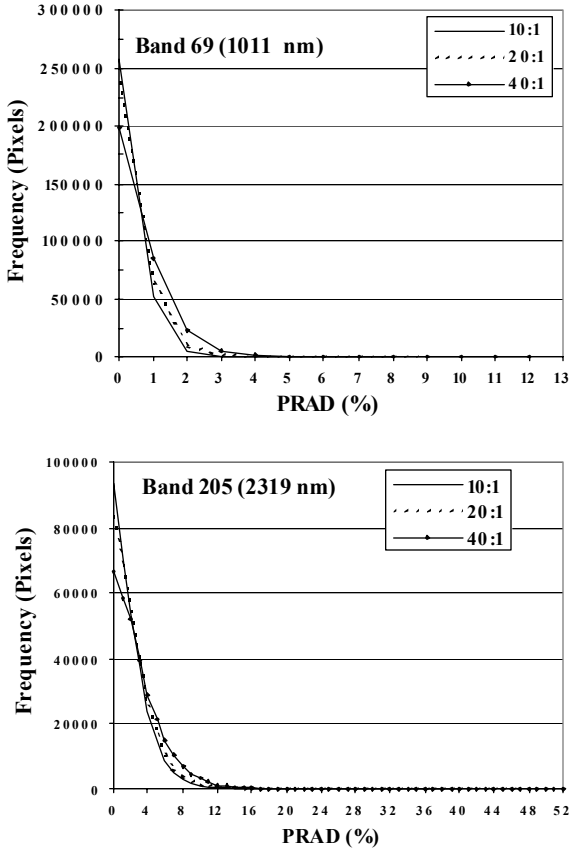

Figure 2. Frequency (pixel) distribution of PRAD for band 69 (1011 nm) and 205 (2319 nm)

The spectral difference (PRAD) between original and de-compressed data for individual pixels behaves similarly to these two fidelity assessment cases. An example derived for an "alunite" pixel for the compression ratios 10:1, 20:1, and 40:1 is shown in Figure 3. It indicates that the relative differences for the 10:1 and 20:1 compression ratios are very similar with errors below 0.3 % in most bands. These errors increase up to 1% above 2398 nm. As expected, errors of up to 6.3 % occur in the strong atmospheric water absorption regions at 1380 nm and 1870 nm. The results, retrieved from the comparison of the original spectrum and the spectrum compressed at 40:1, revealed larger errors, up to 10.2 %, with the strong water absorption regions excluded.

5.2 Data Products

The results of the endmember selection using the IEA approach are summarized in Table 3 for the original and de-compressed data cubes. The endmembers found were identified using the USGS spectral library and mineral map, which was derived from AVIRIS data (USGS, 2002). Compared to the original data, the same endmembers were retrieved from data at compression ratios 10:1 and 20:1, although the IEA procedure selected some of the endmembers in a different order, resulting

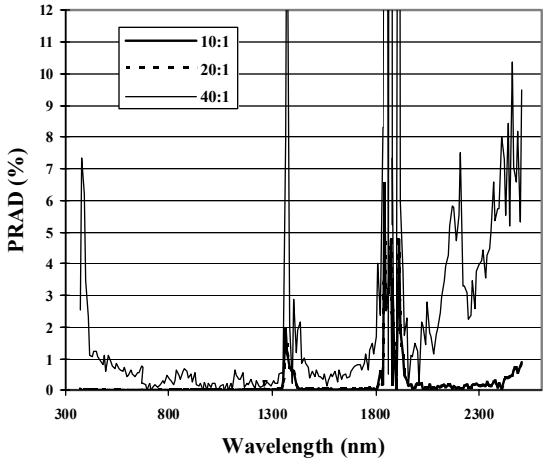

Figure 3. PRAD calculated from original and de-compressed radiance spectra for an "alunite" pixel

in a different endmember number for a given endmember. Accordingly, no endmembers were lost. This is not the case for the 40:1 compression ratio where the endmember 14, dickite (mixed with kaolinite), was not retrieved.

Original EM #	Endmember	10:1 Em #	20:1 EM #	40:1 EM #
1	Chalcedony	1	1	1
2	Calcite (mixed with unknown)	2	2	2
3	Alunite	3	3	3
4	Kaolinite	4	4	4
5	Montmorillonite (mixed with unknown)	5	5	5
6	Dickite	6	6	6
7	Kaolinite	7	7	7
8	Muscovite (mixed with unknown)	8	8	9
9	Kaolinite (mixed with Alunite)	9	9	8
10	Alunite (mixed with Kaolinite)	11	10	11
11	Alunite (mixed with Kaolinite)	10	11	10
12	Buddingtonite	12	12	12
13	Montmorillonite	13	14	13
14	Dickite (mixed with Kaolinite)	14	15	lost
15	Montmorillonite	15	13	15

Table 3. Endmembers extracted from the different cubes with the automatic IEA procedure

Differences between endmember spectra, extracted from original data and decompressed data, generally increase with increasing compression ratio. This trend is reflected by the SAM fidelity measure with average values of 0.004 (compression ration of 10:1), 0.008 (20:1) and 0.010 (40:1) for all the endmembers. However, deviations from this trend occur for muscovite (endmember 8) and for calcite (2) where the SAM values for the 20:1 compression ratio are higher than those at the 40:1 ratio. It should be noted in this context that endmember spectra, extracted from the original data and de-

compressed data, are not necessarily derived from the same pixels, thereby enhancing the probability of spectral differences for a specific endmember. The relatively low SAM values, of up to 0.03 indicate that the typical shapes of the mineral absorption features were preserved for all compression ratios. In order to further illustrate this statement, examples of endmember spectra of kaolinite (endmember 4) and buddingtonite (12) are shown in Figure 4 for the 2000-nm to 2500-nm wavelength range. This is the key range for identification and mapping minerals using hyperspectral data. The fidelity measures SAM and APRAD are listed in Table 4 for these examples. Despite larger errors for buddingtonite (compression ratio of 40:1), its typical absorption feature centred around 2120 nm has been preserved.

Compression Ratio	10:1	20:1	40:1
Kaolinite: SAM	0.004	0.007	0.010
APRAD	0.5	1.1	2.0
Buddingtonite: SAM	0.004	0.04	0.019
APRAD	0.7	0.4	5.9

Table 4. Fidelity measures SAM and APRAD (%) for kaolinite (endmember 4) and muscovite (8)

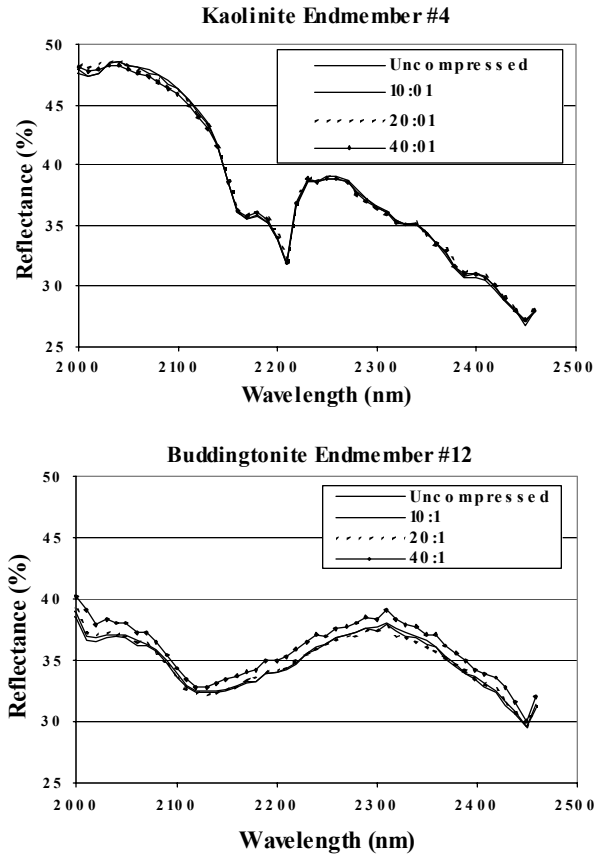

Figure 4. Endmember spectra of kaolinite and buddingtonite for the original and de-compressed data cubes

The RMSE between the fractions, extracted from the original data and de-compressed data, increases with increasing compression ratios as demonstrated in Figure 5. The RMSE averaged over the endmembers amounts to 0.02 (compression ratio of 10:1), 0.03 (20:1), and 0.04 (40:1). The largest percent (relative) differences occur for the low fraction values, which are not an issue since only the high abundances of minerals are of interest for mineral exploration purposes. Therefore, only the fractions above 0.5 were mapped for the individual endmembers as shown in Figure 6 for endmember 5, montmorillonite. It can be seen for the compression ratios 10:1 and 20:1 that the spatial pattern is similar to the one derived from the original data, although some of the pixels are not mapped at all or are incorrectly classified. Despite the increase of these classification errors for the 40:1 compression ratio, the spatial pattern is still recognizable. This is generally also the case for the other endmembers with the exception of endmember 8, muscovite where the abundance maps retrieved from data at the three compression ratio show significant spatial distribution differences compared to the one extracted from the original data.

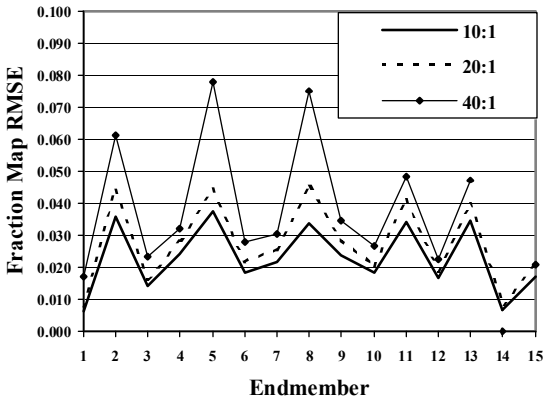

Figure 5. RMSE of the fractions extracted from the original and de-compressed data cubes for the different endmembers. The x-axis refers to the endmember numbering of the original data.

6.0 CONCLUSIONS

The impact of lossy HSOQVQ data compression on mineral mapping was investigated in this paper. The compression ratios 10:1, 20:1, and 40:1 were used to compress AVIRIS radiance data acquired over Cuprite, Nevada. In general, the errors between original and decompressed data, as well as derived products (endmembers, mineral abundances), increase with increasing compression ratio. All of the 15 endmembers, retrieved from the original data, could be extracted from the data compressed at ratios of 10:1 and 20:1. However, one endmember, calcite, was lost for the 40:1 data compression case. This implies that this particular endmember (mineral) could not be mapped. In addition, the spectral differences are larger for the 40:1 compression ratio than for the other two ratios. The same is true for the resulting mineral abundance (fraction) maps. A comparison of abundance maps with fractions larger than 0.5 revealed similar results. These maps show generally a similar spatial pattern for the compression ratios 10:1 and 20:1 as for those derived from the original data. This spatial pattern is still recognizable for most of the endmembers extracted from data at 40:1 data compression ratio, although the classification errors are considerably larger. The preliminary results presented in this paper are encouraging and indicate that data compression ratios of 10:1 and 20:1 are likely suitable for identification and mapping minerals in Cuprite-like environments. These two ratios form the limits within hyperspectral data need to be compressed onboard operational spaceborne systems in order to guarantee the transfer of data in a timely fashion to the ground receiving

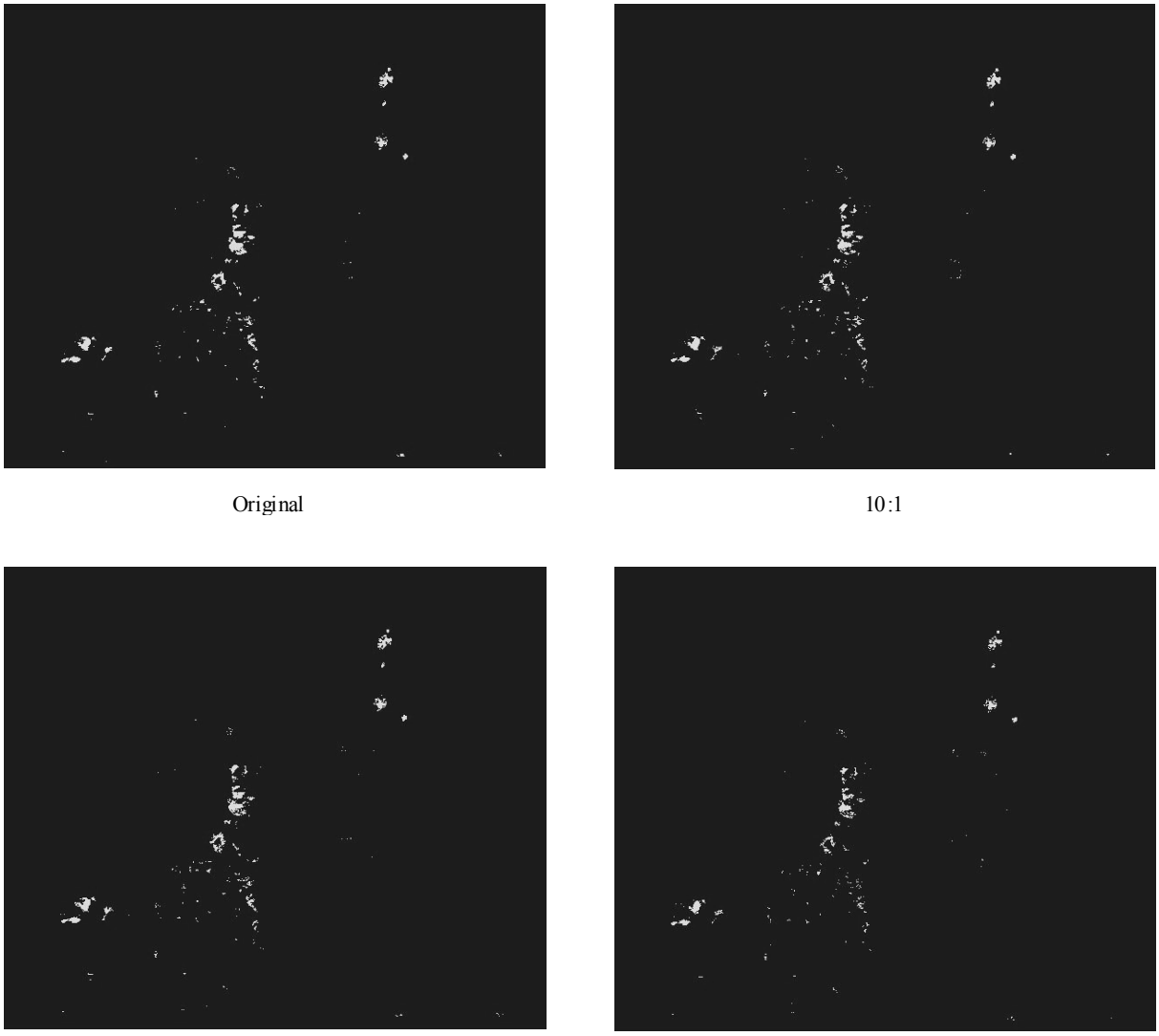

Original 10:1

20:1 40:1

Figure 6. Abundance maps of endmember 5, Montmorillonite, for fractions larger than 0.5

stations. The 40:1 ratio is not acceptable due mainly to the loss of one endmember.

7.0 ACKNOWLEDGEMENT

The authors like to thank NASA's JPL for making the AVIRIS data cube available.

8.0 REFERENCES

Boardman, J.W., 1995. Analysis, Understanding and Visualization of Hyperspectral Data as Convex Sets in n-Space, In: *Proceedings of the International SPIE Symposium on Imaging Spectrometry*, Orlando, Florida, U.S.A., SPIE Vol. 2480, pp. 23-36.

Goetz, A.F.H., and V. Srivastava, 1985. Mineralogic Mapping in the Cuprite Mining District, Nevada, In: *Proceedings of the First AIS Workshop,* Pasadena, California, U.S.A., JPL-Publication 85-41, pp. 22-31.

Green, R.O., M.L. Eastwood, C.M. Sarture, T.G. Chrien, M. Aronsson, B.J. Chippendale, J.A. Faust, B.A. Pavri, C.J. Chovit, M. Solis, M.R. Olah, and O. Williams, 1998. Imaging Spectroscopy and the Airborne Visible/Infrared Imaging Spectrometer (AVIRIS). *Remote Sensing of Environment,* 65, pp. 227-248.

Hook, S.J., and M. Rast, 1990. Mineralogic Mapping Using Airborne Visible/Infrared Imaging Spectrometer (AVIRIS) Shortwave Infrared (SWIR) Data Acquired over Cuprite, Nevada, In: *Proceedings of the Second Airborne Visible/Infrared Imaging Spectrometer (AVIRIS) Workshop*, Pasadena, California, U.S.A., JPL Publication 90-54, pp. 199-207.

Kruse, F.A., A.B. Lefkoff, and J.B. Dietz, 1993. Expert System-Based Mineral Mapping in Northern Nevada Death Valley, California/Nevada, Using the Airborne Visible/Infrared Imaging Spectrometer (AVIRIS), *Remote Sensing of Environment*, 44, pp. 309-336.

Neville, R.A., J. Lévesque, K. Staenz, C. Nadeau, P. Hauff, and G.A. Borstad, 2003. Spectral Unmixing of Hyperspectral Imagery for Mineral Exploration: Comparison of Results from SFSI and AVIRIS. Canadian Journal of Remote Sensing, (in press).

Press, W.H., S.A. Teukolsky, W.T. Vetterling, and B.P. Flannery, 1902. *Numerical Recipes in C*. Cambridge University Press, Cambridge, England, pp. 123-125.

Qian, S-E., A.B. Hollinger, D. Williams, and D. Manak, 1997. 3D Data Compression System Based on Vector Quantization for Reducing the Data Rate of Hyperspectral Imagery. *Applications of Photonic Technology 2*, Plenum Press, New York, U.S.A., pp. 641-654.

Qian, S-E., A.B. Hollinger, D. Williams, and D. Manak, 2000. Vector Quantization Using Spectral Index Based Multiple Sub-Codebooks for Hyperspectral Data Compression. *IEEE Transaction on Geoscience and Remote Sensing*, 38(3), pp. 1183-1190.

Qian, S-E., B. Hu, M. Bergeron, A. Hollinger, and P. Oswald, 2002. Quantitative Evaluation of Hyperspectral Data Compressed by Near Losless Onboard Compression Techniques. In: *Proceedings of the International Geoscience and Remote Sensing Symposium (IGARSS)*, Toronto, Ontario, Vol. III, pp. 1425-1427.

Shimabukuru, Y.E., and J.A. Smith, 1991. The Least Squares Mixing Models to Generate Fraction Images Derived From Remote Sensing on Multispectral Data, *IEEE Transactions on Geoscience and Remote Sensing*, 29, pp. 16-20.

Staenz, K., and D.J. Williams, 1997. Retrieval of Surface Reflectance from Hyperspectral Data Using a Look-Up Table Approach. *Canadian Journal of Remote Sensing*, 23(4), pp. 354-368.

Staenz, K., T. Szeredi, R.J. Brown, H. McNairn, and R. VanAcker, 1997. Hyperspectral Information Extraction Techniques Applied to Agricultural *casi* Data for Detection of Within-Field Variations, In: *Proceedings of the International Symposium in the Era of Radarsat and the Nineteenth Canadian Symposium on Remote Sensing*, Ottawa, Ontario, Canada, 8 pages (CD-ROM).

Staenz, K., T. Szeredi, and J. Schwarz, 1998. ISDAS - A System for Processing/Analyzing Hyperspectral Data, *Canadian Journal of Remote Sensing*, 24(2), pp. 99-113.

Staenz, K., R.A. Neville, J. Lévesque, T. Szeredi, V. Singhroy, G.A. Borstad, and P. Hauff, 1999. Evaluation of *casi* and SFSI Hyperspectral Data for Environmental and Geological Applications – Two Case Studies, *Canadian Journal of Remote Sensing*, 25(3), pp. 311-322.

Swayze, G., R.N. Clark, F. Kruse, S. Sutley, and A. Gallagher, 1992. Ground-Truthing AVIRIS Mineral Mapping at Cuprite, Nevada, In: *Summaries of the Third Annual JPL Airborne Geoscience Workshop*, Pasadena, California, U.S.A., JPL Publication 92-14, Vol. 1, pp. 47-49.

Szeredi, T., K. Staenz, and R.A. Neville, 2002. Automatic Endmember Selection: Part I Theory, *Remote Sensing of Environment*, (submitted).

USGS, 2002. USGS Digital Spectral Library, Denver, Colorado, U.S.A.
http://speclab.cr.usgs.gov/spectral-lib.html